Structure of micro-crack population and damage evolution in concrete

Andrey P Jivkov[1,*]

[1] School of Mechanical, Aerospace and Civil Engineering, The University of Manchester, Manchester M13 9PL, UK
* Corresponding author: andrey.jivkov@manchester.ac.uk

Abstract Tensile behaviour of concrete is controlled by the generation and growth of micro-cracks. A 3D lattice model is used in this work for generating micro-crack populations. In the model, lattice sites signify solid-phase grains and lattice bonds transmit forces and moments between adjacent sites. The meso-scale features generating micro-cracks are pores located at the interfaces between solid-phase grains. In the model these are allocated to the lattice bonds with sizes dictated by an experimentally determined pore size distribution. Micro-cracks are generated by removal of bonds when a criterion based on local forces and pore size is met. The growing population of micro-cracks results in a non-linear stress-strain response, which can be characterised by a standard damage parameter. This population is analysed using a graph-theoretical approach, where graph nodes represent failed bonds and graph edges connect neighbouring failed bonds, i.e. coalesced micro-cracks. The evolving structure of the graph components is presented and linked to the emergent non-linear behaviour and damage. The results provide new insights into the relation between the topological structure of the population of micro-cracks and the macroscopic response of concrete. They are applicable to a range of quasi-brittle materials with similar dominant damage mechanisms.

Keywords Concrete porosity; Lattice model; Cracking graphs; Macroscopic damage

1. Introduction

The mechanical behaviour of quasi-brittle materials, such as concrete, graphite, ceramics, or rock, emerges from underlying microstructure changes. At the engineering length scale it can be described with continuum constitutive laws of increasing complexity combining damage, plasticity and time-dependent effects [1-4]. In these phenomenological approaches the damage represents reduction of the material elastic constants. From the microstructure length scale perspective damage is introduced by the nucleation and evolution of micro-cracks. While the population of micro-cracks formed under loading could be sufficiently well captured by various continuum damage models, the latter cannot help to understand the effects of the population on other important physical properties of the material. In many applications the quasi-brittle materials have additional functions as barriers to fluid transport via convection/advection and/or diffusion. It is therefore important to take a mechanistic view on the development of damage by modelling the evolution of micro-crack population, which can inform us about changes in the transport properties. Such a mechanistic approach needs to account for the material microstructure in a way corresponding to the mechanism of micro-crack formation [5]. Micro-cracks typically emerge from pores in the interfacial transition zone between cement paste and aggregate in cement-based materials [6].

Discrete lattice representation of the material microstructure seems to offer the most appropriate modelling strategy for analysis of micro-crack populations. This is a meso-scale approach, where the material is appropriately subdivided into cells and lattice sites are placed at the centres of the cells. Discrete lattices allow for studies of distributed damage without constitutive assumptions about crack paths and coalescences that would be needed in a continuum finite element modelling. The deformation of the represented continuum arises from the interactions between the lattice sites. These involve forces resisting relative displacements and moments resisting relative rotations between sites. Two conceptually similar approaches have been proposed to link local interactions to continuum response. In the first one, the local forces are related to the stresses in the continuum cell, e.g. [7, 8]. In the second one, the interactions are represented by structural beam elements, the stiffness coefficients of which are determined by equating the strain energy in the discrete and the continuum cell, e.g. [9, 10]. In both cases explicit relations between local and continuum parameters can be established for regular lattices [11], but the only isotropic material that can be represented in 3D is a material with zero Poisson's ratio. A bi-regular lattice that can represent all materials of practical interest has been proposed recently [12]. This lattice, currently formed by beams clamped at sites, is used in the current work together with microstructure data for concrete obtained with X-ray computed tomography. Failure models based on microstructure data and the new lattice have been previously used for modelling tensile and compressive behaviour of cement [13] and the compressive behaviour of concrete under various complex loading conditions [14]. This work makes a step into developing our understanding of the micro-crack population and its relation to macroscopic damage.

Most of the work relating micro-crack populations to elastic moduli follows the fundamental paper [15], where analytical statistical derivation of the relation was provided. We follow the interpretation given in [16], in which the damage is measured as a relative change of the elastic modulus and related to micro-crack population via

$$D = 1 - \frac{E}{E(0)} = \frac{\beta}{N_T} \sum_{c \geq 1} c^3 N(c), \tag{1}$$

where c is some measure of micro-crack size, $N(c)$ is the number of micro-cracks of size c, N_T is the total number of sites capable of nucleating micro-cracks, and β is a scaling parameter reported as 0.47π for cracks in a 2D medium. Eq. (1) is our point of comparison for the simulations performed with the lattice model for various tensile loading cases. In the current work we are interested in testing the range of applicability of Eq. (1) and understanding the reasons for deviation from this rule, should such occur, by explicitly analysing the micro-crack population growth.

2. Model and method

2.1. The site-bond model

The lattice model used in this work is illustrated in Fig. 1. The unit cell, shown in Fig. 1(a) is a truncated octahedron – a solid with six square and eight regular hexagonal boundaries. The 3D space can be compactly tessellated using such cells, with each cell representing a material meso-scale feature, e.g. grain, in an average sense. This representation is supported by physical and statistical arguments [12]. A discrete lattice is formed by placing sites at the centres of the cells and connecting each site to its 14 nearest neighbours; example is shown in Fig. 4(b). The lattice contains two types of bonds. Bonds denoted by B_1 are normal to square boundaries and form orthogonal set. For convenience this set is coincident with the global coordinate system and B_1 are referred to as principal bonds. Bonds denoted by B_2 are normal to hexagonal boundaries. The hexagons lie on the octahedral planes with respect to the selected system, hence B_2 are referred to as octahedral bonds.

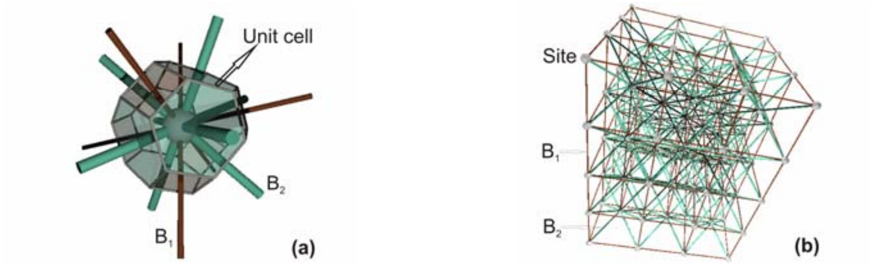

Figure 1. Lattice illustration: (a) Unit cell showing the site with 14 coordinating bonds: six principal, B_1, and eight octahedral, B_2; (b) Discrete lattice of beam elements.

If the spacing between sites in the principal directions is denoted by L, bonds B_1 have length $L_1 = L$, and bonds B_2 have length $L_2 = \sqrt{3}\ L / 2$. Presently, the bonds are represented by structural beam elements of circular cross sections, with R_1 and R_2 denoting the radii of beams B_1 and B_2, respectively. The beams are clamped at the lattice sites. The two types of beams have identical modulus of elasticity, E_b, and Poisson's ratio, ν_b. With this setup, it has been previously shown that by calibrating four parameters: R_1 / L, R_2 / L, E_b, and ν_b, the lattice can produce a large class of isotropic elastic materials with Poisson's ratios of practical interest [12]. The reference material in this work is a concrete with $E = 46$ GPa and $\nu = 0.27$, for which the calibration, assuming isotropic elasticity, yields $R_1 / L = 0.2$; $R_2 / L = 0.32$; $E_b = 90$ GPa; and $\nu_b = 0.4$ [14]. The commercial software Abaqus [17] with Euler-Bernoulli beam formulation has been used for the calibration and the analyses reported in this work. The behaviour of the beams is linear elastic.

2.2. Pore distribution and failure criterion

Microstructure data for the reference material was obtained using X-ray Computed Tomography as reported in [14]. The pore size distribution was obtained by segmentation of reconstructed 3D images. The studied regions of interest had dimensions of 1700 x 1200 x 1200 voxels with a voxel size of ca. 15 μm, allowing for a minimum detectable pore radius of ca. 15 μm. The number of pores measured experimentally was $n \approx 41500$. The measured pore radii, c_i, were used to construct a cumulative probability distribution (CPD) with standard median ranking, where for pore radii ordered as $c_1 \leq c_2 \leq \ldots \leq c_n$, the cumulative probability for pores with radii less than c_i is given by $F(c < c_i) = (i - 0.3) / (n + 0.4)$. The CPD for the reference material is shown in Fig. 2(a), where the minimum and maximum pore radii are also depicted. The CPD is used to assign pore sizes to the lattice bonds. For each bond a uniformly distributed random number $0 \leq r < 1$ is generated and the assigned pore radius is calculated from $c = F^{-1}(r)$. This ensures that the distribution of pore sizes in the model comes from the same population as in the experiment. A fragment of the model with distributed pores is given in Fig. 2(b). The cell size, L, is calculated such that the volume of all distributed pores divided by the volume of the cellular structure equals the material porosity, which is ca. 5% for the reference material. The pore sizes shown are to scale with the sketched cellular structure. With respect to the cellular structure pores reside at cell boundaries, i.e. interfaces between grains. The lattice bonds are also depicted (diameters not to scale) in order to show that pores reside at bond centres.

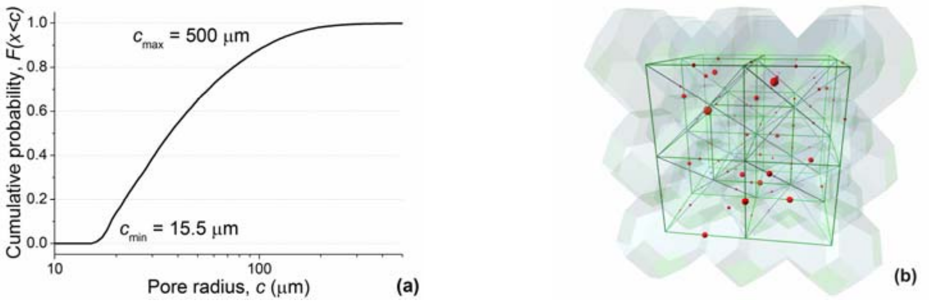

Figure 2. Pore distribution: (a) Cumulative probability of pore radii in the concrete; (b) Segment of model illustrating pores distributed to cell boundaries and corresponding. Pore sizes are to scale with the cell size.

Damage in the lattice model is introduced by removal of bonds. Propensity for bond failure is measured by the parameter

$$\Pi = \frac{N}{N_f} + \frac{|S|}{S_f} + \frac{|T|}{T_f} + \frac{|M|}{M_f}, \tag{2}$$

where N and S are the normal and shear forces in the beam; T and M are the twisting and bending moments; N_f, S_f, T_f, and M_f are critical values. N is positive for tension and negative for compression. S and M are obtained from the values in the two directions normal to the beam axis using the square root of squares rule. Eq. (2) provides an interaction between the different forces that allows for failure when $\Pi \geq 1$ under the combined action of normal and shear stresses [18, 14]. Taking only the first and fourth term was previously used in criteria with no account for shear, e.g. [19]. The second and third term allow for shear failure similarly to [10]. The failure parameters N_f, S_f, T_f, and M_f can be related [18]. For a beam of circular cross section of radius R, the tensile failure stress is $\sigma_f = N_f / (\pi R^2)$. The maximum bending stress is $\sigma_{max} = 4M / (\pi R^3)$, which equals σ_f when $M_f = N_f R / 4$. Similarly, the shear failure stress is $\tau_f = S_f / (\pi R^2)$. The maximum torsion stress is $\tau_{max} = 2T / (\pi R^3)$, which equals τ_f when $T_f = S_f R / 2$. Thus Π requires two material parameters: σ_f and τ_f. Noting that for quasi-brittle materials typically $1 \leq \tau_f / \sigma_f \leq 2$ [18], in this work $\tau_f = 2\sigma_f$ is used, representing more brittle materials.

The tensile failure strength of a bond, σ_f, is related to the size of the pore assigned to the bond. The relation used here is simpler than in the previous work [14] and based on the assumption that σ_f is the beam remote stress for which the average stress in the beam ligament outside the pore attains a critical value σ_0. Thus

$$\sigma_f = \sigma_0 \left[1 - \left(\frac{c}{R} \right)^2 \right], \tag{3}$$

where c and R are the pore and beam radii, respectively, and σ_0 can be interpreted as the tensile strength of the material without a defect. With this setup and the choice $\tau_f = 2\sigma_f$ the failure model requires a calibration of a single parameter, σ_0, against experimental stress-strain curve. However, since the beams behaviour is linear elastic, the choice of σ_0 would affect only the calculated macroscopic stresses but not the order in which damage (beam failures) would evolve in the system. Because the interest here is investigating the evolution of damage, σ_0 = 1 MPa is used for the calculations, noting that macroscopic stress response can be simply scaled by another value of σ_0.

2.3. Load cases and solution

A model of size ($20L$, $20L$, $20L$) was used. The lattice contained 17261 sites and 113260 bonds: 49260 B_1 and 64000 B_2. The coordinate system (X_1, X_2, X_3) was coincident with B_1, so that the boundary planes $X_1 = 0$, $X_1 = 20L$, $X_2 = 0$, $X_2 = 20L$, $X_3 = 0$, $X_3 = 20L$ contained 21×21 sites (nodes). Boundary conditions normal to each plane were only applied. Thus U_i and F_i denote displacements and forces of nodes on plane with normal X_i, while other displacements and rotations on this plane were unconstrained. Table 1 shows the conditions on planes $X_1 = 20L$, $X_2 = 20L$, and $X_3 = 20L$ for the analysed cases. Additionally, $U_1 = 0$ on $X_1 = 0$; $U_2 = 0$ on $X_2 = 0$; $U_3 = 0$ on $X_3 = 0$, apply to all.

Table 1. Boundary conditions for loading cases.
Values given in bold denote applied conditions. A stands for values obtained from finite element analyses.

Case	U_1	U_2	U_3	F_1	F_2	F_3	Note
C1	$\boldsymbol{d_1}$	A	A	A	**0**	**0**	Uniaxial unconfined extension
C2	$\boldsymbol{d_2}$	$\boldsymbol{d_2}$	A	A	A	**0**	Plane stress
C3	$\boldsymbol{d_3}$	$\boldsymbol{d_3}$	**0**	A	A	A	Plane strain
C4	$\boldsymbol{d_4}$	**0**	**0**	A	A	A	Uniaxial confined extension

For cases where nodal reaction forces were determined from analysis, the macroscopic stress in the respective direction was calculated as the ratio between the total reaction force and the boundary area, i.e. $\sigma_i = \Sigma F_i / 400L^2$. For the cases where nodal displacements were determined from analysis, the macroscopic strain in the respective direction was calculated as the ratio between the average displacement and the model length, i.e. $\varepsilon_i = \Sigma U_i / (21^2 \times 20L)$.

The evolution of damage was simulated by failure of bonds, controlled by an in-house code, and repetitive solution for equilibrium performed by Abaqus with constant applied displacements. The values of $\boldsymbol{d_i}$ were selected so that the strain energy density in the system prior to damage was one for the four cases for the purpose of comparison. At each step the in-house code obtains the forces and moments in all bonds and calculates the propensity for failure, Π, for each bond. The bond with maximum Π is then removed and the updated lattice is solved for equilibrium. This leads to redistribution of forces for the continuous damage evolution. The magnitudes of Π at which consecutive failures occurred can be used to cut-back the applied strain and resulting stress and obtain a macroscopic stress-strain response. The focus of this work is not on determining the stress-strain response, but on the relation between damage and crack population. To this end we define four damage parameters, measuring the relative changes of the hydrostatic stress and the three components of the stress deviator by:

$$D_H = 1 - \frac{\sigma_H}{\sigma_H(0)}; \quad D_i = 1 - \frac{S_i}{S_i(0)}, \quad where \quad S_i = \sigma_i - \sigma_H, \, i = 1,2,3 . \tag{4}$$

Note that for isotropic deformation and damage these parameters must be equal and equivalent to the damage parameter defined via relative reduction of Young’s modulus or shear modulus.

2.4. Crack population analysis

A bond failure is thought of as a micro-crack nucleation, specifically as a separation between the adjacent cells in the cellular structure along their common face. Initially, the micro-cracks may be dispersed in the model reflecting the random distribution of pore sizes and the low level of interaction due to force redistribution. Interaction and coalescence may follow as the population of micro-cracks increases. The structure of the failed surface can be represented with a mathematical graph, where graph nodes represent failed faces and graph edges exist between failed faces with common triple line in the cellular structure, i.e. where two micro-cracks formed a continuous larger crack. Generally, the graph of a failed surface is a disconnected set of sub-graphs or components, some of which could be single nodes as at the start of damage evolution, while others could be connected sets representing larger micro-cracks as the coalescence develops. For the analysis, nodes are equipped with weights equal to the failed face areas. Edges are equipped with weights equal to the shortest path along connected faces between their centres.

The components of a failed surface graph are sorted into sets according to their areas $A_1 < A_2 \ldots < A_k$, so that each set contains N_i disconnected components of area A_i. The linear size of a component is approximated with the square root of its area so that the moment of the crack population is formed using (compare to Eq. (1))

$$M = \frac{1}{A_T} \sum_{i=1}^{k} A_i^{3/2} N_i \,, \tag{5}$$

where A_T is the total area of the faces in the cellular structure. This can in principle be replaced with a linear measure to conform to Eq. (1). A realistic choice is to use the component diameter which is the maximal shortest path between component’s nodes calculated with the weighted edges. The process, however, is computationally expensive and does not lead to noticeable changes in the results for the cases analysed here. Eq. (5) is used after each failure event to calculate the evolution of the moment with damage. In addition, the maximal component is monitored. This is the largest connected cracked surface.

3. Results and discussion

Figure 3 shows the results of the evolution of the damage parameters defined by Eq. (4) as functions of the moment of crack population defined by Eq. (5). Recall that a damage parameter, based on the relative change of the Young's modulus equals the damage parameters based on the individual stress components, deviatoric and hydrostatic, when the material remains macroscopically isotropic. In this case the same damage parameter describes the relative change of the shear modulus. The results for the cases of uniaxial extension, unconfined (a) and confined (d), show equality of the four damage parameters (approximate in case 4). This suggests that microscopic isotropy is maintained during damage evolution and the results reproduce very closely the linear relation predicted by the theory and given by Eq. (1). Interestingly, an estimate for the slope of the linear function from the figures is about 1.5, which is very close to the value of β reported in relation to Eq. (1).

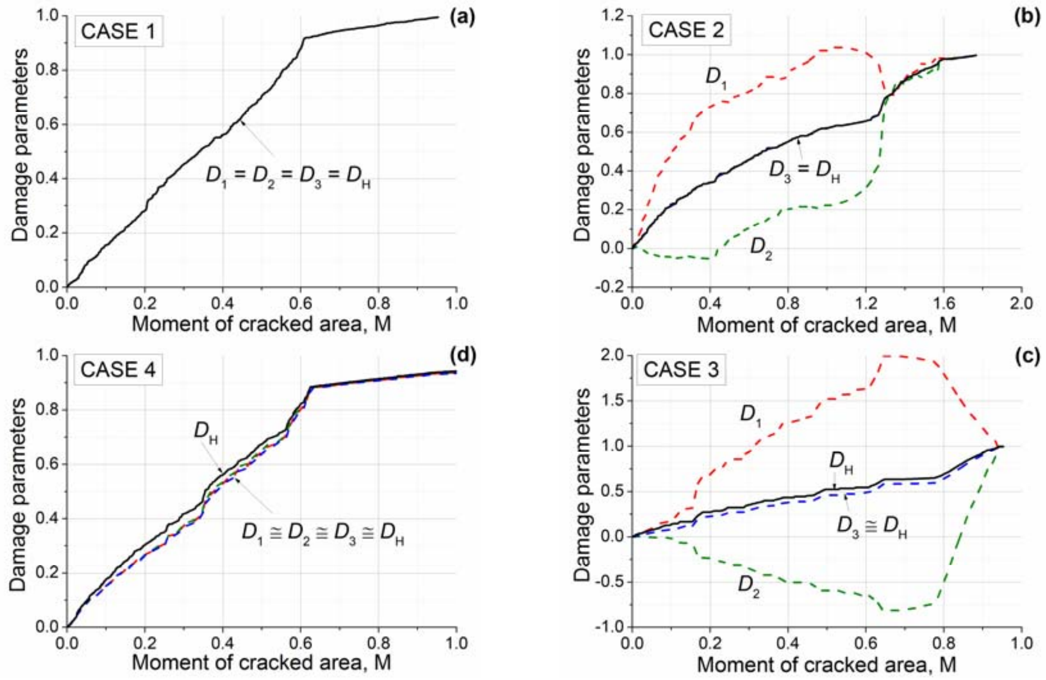

Figure 3. Damage parameters relation to crack population moment.

In the cases of plane stress (b) and plain strain (c), however, the development of damage is radically different, illustrating the development of damage-induced anisotropy. In this case the damage parameter D_i represents the relative reduction of the longitudinal shear modulus in direction X_i. Note that this is not the shear modulus relating shear stress to shear strain. In both plane cases, the evolution of D_1 suggest that the system undergoes transition into negative longitudinal shear resistance, quite more pronounces in the plane strain case (c), while the shear resistance in direction X_2 increases from its initial value. This behaviour may seem unusual, but it is not impossible for anisotropic materials. The bounds for Poisson's ratios in such materials calculated in [20, 21] allow for negative longitudinal shear moduli with the values recorded here. The results merely show that extreme anisotropy has been developed in the material with the evolution of micro-crack population under the two plane cases. The development of the hydrostatic damage is also affected in these cases, as it cannot be described as a linear function of the cracked area moment.

To understand what causes the anisotropy in the plane cases the structure of the crack population needs to be studied in more detail. This requires a single damage parameter; an appropriate choice is the relative reduction of the strain energy density in the system, $D = 1 - W / W(0)$, which is found to be approximately equal to the damage parameter defined via the relative reduction of the hydrostatic stress in all cases, see Fig. 4(a). The development of the maximal graph component, i.e. the main crack, with damage is shown in Fig. 4(b) with the ratio between the area of the maximal component, A_m, to the total cracked area, A. It is clear that the main crack becomes dominant very early in the development of damage (at damage less than 1%) and its relative area grows nearly exponentially for all cases. It seems therefore sufficient to examine the structure of the maximal component as the damage develops.

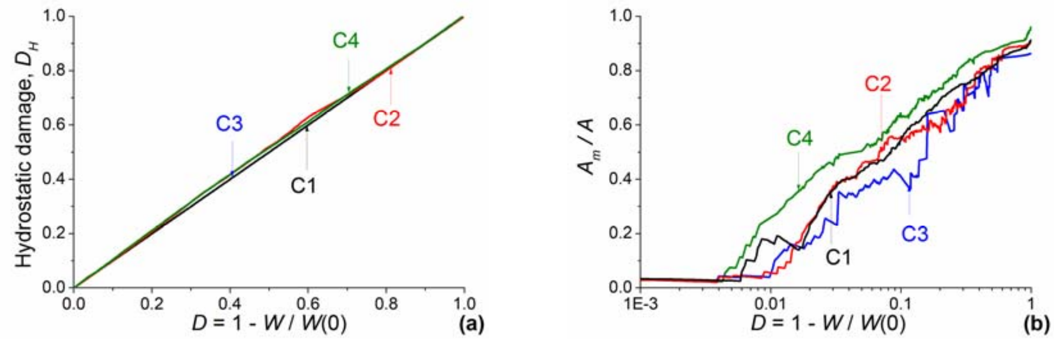

Figure 4. Hydrostatic damage (a) and relative area of main crack (b) development with damage defined as relative reduction of strain energy density.

Figure 5 shows the development of the maximal component area, split into the areas of surfaces normal to the three principal axes, A_1, A_2, A_3, and the surfaces formed on octahedral planes, A_4. All areas are normalised with the total areas of the corresponding boundaries in the cellular structure. In the cases of uniaxial extension, unconfined (a) and confined (d), the development of the main crack involves creation of surfaces normal to the applied load and on octahedral planes. Although there is a difference between the two cases in the rates of creation of normal and octahedral surfaces, the overall balance results in isotropic damage, see Fig. 3(a),(d).

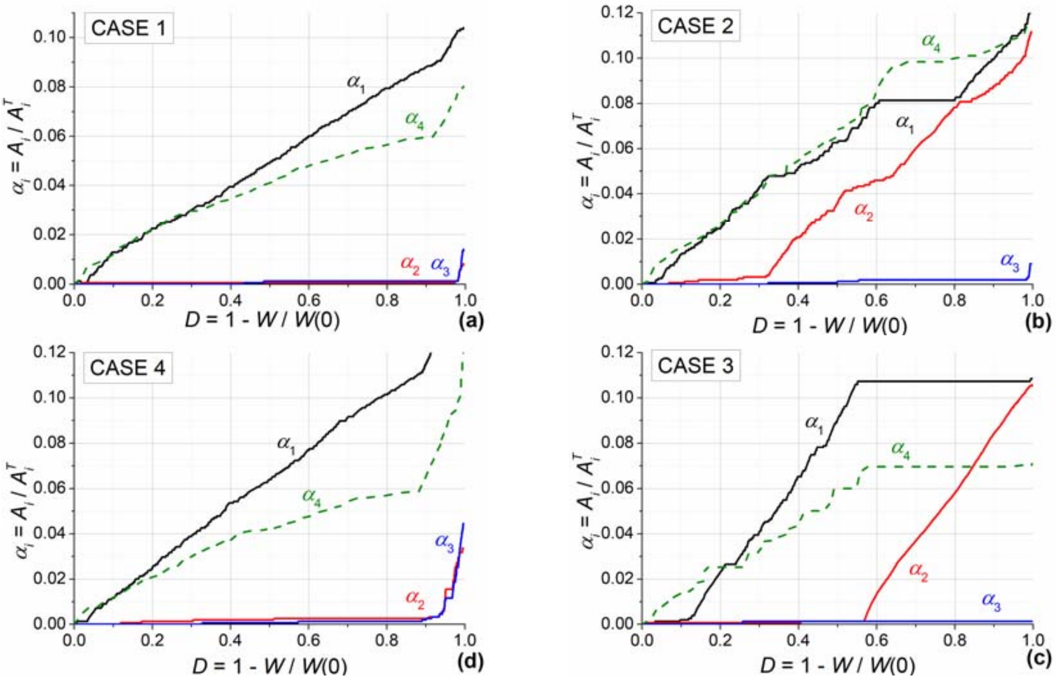

Figure 5. Structure of maximal graph component with damage.

In the plane stress (b) and plane strain (c) cases, the development of the main crack follows very different patterns. The parallel increase of normal to the first loading axis and octahedral surfaces in plane stress, Fig. 5(b), seems to be responsible for the immediate development of damage-induced anisotropy, which after that appears to be moderated by the development of surfaces normal to the second loading axis. The constraint in plane strain, Fig. 5(c), leads to a delayed but rapid increase of surfaces normal to the first loading axis together with a lower rate of creation of octahedral surfaces. This appears to delay substantially the development of cracked surfaces normal to the second loading axis and results in significantly higher anisotropy.

It should be noted that the structure-damage relations reported here were found qualitatively independent of the random assignment of pores in the lattice model as well as of the shape parameter of the pore distribution. This has been confirmed by a number of simulations with different shape of distribution and random assignments. One parameter that may affect the outcomes is the shear to normal strength ratio; this is a subject of ongoing work. It is further understood that the outcomes reported here are principally related to the selected lattice connectivity. However, the detail to which the surface topography can be studied is higher than the detail allowed by models based on cubic lattices. One unknown in the analysis is whether the crack development in the lattice is energetically equivalent to the development of continuum cracks. This question remains to be addressed in a future work. The current observations suggest that a common, constraint independent, damage evolution law might not be feasible to achieve. In such case it seems that a lattice-based analysis might be necessary as a sub-modelling approach to inform the behaviour of finite elements in a continuum model.

The last question of interest in this work is related to the use of the weakest-link statistics for global failure predictions. It was suggested in [16] that weakest-link should be applied to the population of micro-cracks in the system. However, from the simulations performed here it is evident that a single crack, the maximal connected component of the cracked surface, becomes rapidly dominating the behaviour, Fig. 4(b), with few much smaller components disconnected from the main crack. This does not allow for invoking the weakest-link as a descriptor of final failure.

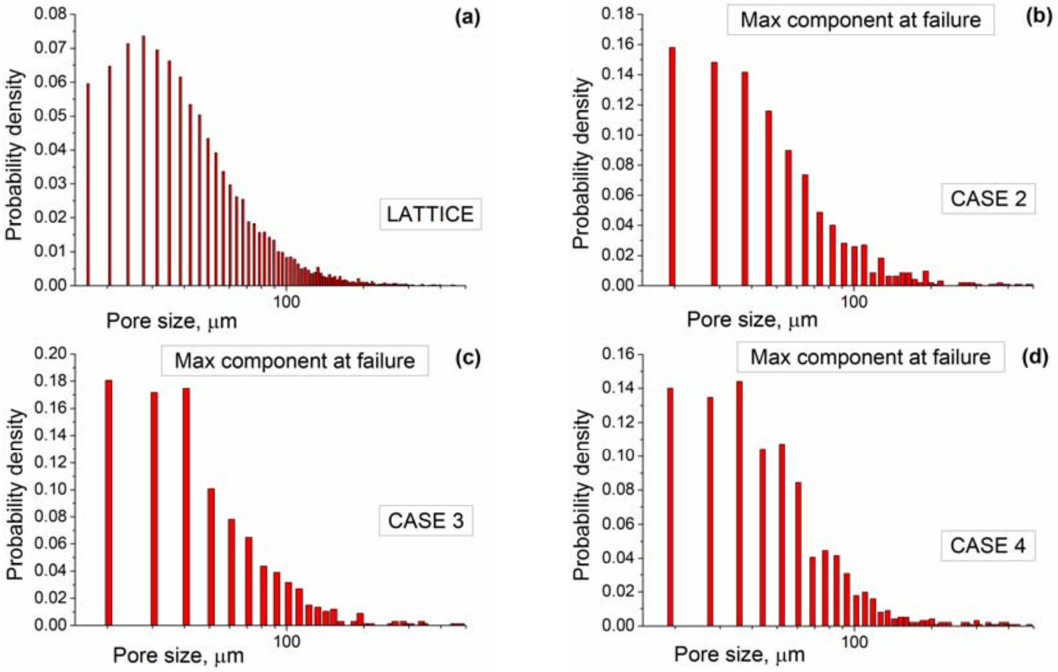

Figure 6. Probability density of pore sizes in the lattice (a) and in the maximal component at failure for three loading cases (b)-(d). Results obtain with the same distribution given by (a).

Another approach would be to base the weakest-link statistics on the microstructure information, in this case the size distribution of crack-initiation features, the pores. This is similar to the approach used in the modelling of cleavage fracture, where second-phase particles are considered to be cleavage initiators. In order to show whether this is a realistic approach, a comparison is made between the probability density of pore sizes distributed in the lattice and pore sizes contained in the maximal component at failure. The results are shown in Fig. 6 for the pores in the entire lattice (a) and three of the loading cases as depicted. The results shown correspond to one and the same random assignment of pore sizes. Evidently, the probability density of the pores belonging to the final fracture surface is different from the lattice distribution and depends on the loading mode. While the initial damage may start at one and the same location in the system, the nature of loading develops the main crack in different ways and the final failure cannot be described as a weakest-link event using the statistics of the sizes of the failure initiation sites. This makes it difficult to derive a load-independent, purely micro-structure based relation between the macroscopic damage and the probability of failure. The outcome supports further the suggestion that macroscopic failure analysis needs to be performed with an underlying lattice-based analysis of local micro-crack propagation.

4. Conclusions

- A microstructure-informed strategy for analysis of damage evolution in quasi-brittle materials was presented, whereas damage results from the formation, growth and interaction of a population of micro-cracks.
- It was demonstrated that in cases of non-uniaxial extension, such as plane stress or plane strain found ahead of a main crack, the micro-crack population development was responsible for elastic anisotropy with extreme variations of longitudinal shear moduli.
- It was shown that the damage-induced anisotropy was a complex function of the crack population structure. A load-independent damage evolution law might not be achievable and explicit analysis of crack population development, e.g. using a lattice model, might be necessary to complement continuum finite element analysis of failure.
- It was shown that the maximal connected component of the crack population, i.e. the largest crack, became dominant very early in the process of macroscopic damage and controlled the ultimate failure. The analysis if this component suggested that the global failure could not be treated as a weakest-link event.
- The graph-theoretical approach to the analysis of micro-crack populations showed significant potential to reveal the underlying topological structure of the cracked surface. Further work is required to link the topological structure to a measure for global probability of failure.

Acknowledgements

The author is grateful to EPSRC for the support for this work via grant EP/J019763/1, as well as to BNFL for the endowment allowing his continuous research.

References

[1] G. Pijaudier-Cabot, Z.P. Bazant, Nonlocal damage theory. J Eng Mech 113 (1987) 1512-1533.

[2] J.W. Ju, On energy-based coupled elastoplastic damage theories: constitutive modelling and computational aspects. Int J Solids Struct 25 (1989) 803-833.

[3] P. Grassl, M. Jirasek, Damage-plastic model for concrete failure. Int J Solids Struct 43 (2006) 7166-7196.

[4] J. Cervenka, V. Papanikolaou, Three dimensional combined fracture-plastic material model for concrete. Int J Plasticity 24 (2008) 2192–2220.

[5] H.S. Wong, M. Zobel, N.R. Buenfeld, R.W. Zimmerman, Influence of the interfacial transition zone and microcracking on the diffusivity, permeability and sorptivity of cement-based materials after drying. Mag Concr Res 61 (2009) 571-589.

[6] K.L. Scrivener, A.K. Crumbie, P. Laugesen, The interfacial transition zone (ITZ) between cement paste and aggregate in concrete. Interface Sci 12 (2004) 411–421.

[7] Z.P. Bazant, B.H. Oh, Microplane model for progressive fracture of concrete and rock. J Eng Mech 111 (1985) 559-582.

[8] G. Cusatis, Z.P. Bazant, L. Cedolin, Confinement-shear lattice CSL model for fracture propagation in concrete. Comp Meth Appl Mech Eng 195 (2006) 7154-7171.

[9] D.V. Griffiths, G.G.W. Mustoe, Modelling of elastic continua using a grillage of structural elements based on discrete element concepts. Int J Numer Meth Eng 50 (2001) 1759-1775.

[10] C.S. Chang, T.K. Wang, L.J. Sluys, J.G.M. van Mier, Fracture modeling using a micro structural mechanics approach - I. Theory and formulation. Eng Fract Mech 69 (2002)1941-1958.

[11] Y. Wang, P. Mora. Macroscopic elastic properties of regular lattices. J Mech Phys Solids 56 (2008) 3459-3474.

[12] A.P. Jivkov, J.R. Yates, Elastic behaviour of a regular lattice for meso-scale modelling of solids. Int J Solids Struct 49 (2012) 3089–3099.

[13] A.P. Jivkov, M. Gunther, K.P. Travis. Site-bond modelling of porous quasi-brittle media. Mineral Mag 76 (2012) 94-99.

[14] A.P. Jivkov, D.L. Engelberg, R. Stein, M. Petkovski, Pore space and damage evolution in concrete. Eng Fract Mech (2013) accepted.

[15] B. Budiansky, R.J. O'Connell, Elastic moduli of a cracked solid. Int J Solids Struct 12 (1976) 81-97.

[16] W.A. Curtin, H. Scher, Time-dependent damage evolution and failure in materials. I. Theory. Phys Rev B 55 (1997) 12038-12050.

[17] ABAQUS 6.11, DS Simulia Corp., 2011.

[18] Y. Wang, S. Abe, S. Latham, P. Mora, Implementation of particle-scale rotation in the 3D-lattice solid model. Pure Appl Geophys 163 (2006)1769-1785.

[19] E. Schlangen, J.G.M van Mier, Experimental and numerical analysis of micromechanisms of fracture of cement-based composites. Cement Concr Compos 14 (1992) 105-118.

[20] A.N. Norris, Extreme values of Poisson's ratio and other engineering moduli in anisotropic materials. J Mech Mater Struct 1 (2206) 793–812.

[21] C.Y. Guo, L.T. Wheeler, Extreme Lamé compliance in anisotropic crystals. Mat Mech Solids 14 (2009) 403-420.